The Role of Higher CO-Multipole Moments in Understanding the Dynamics of Photodissociated Carbonmonoxide in Myoglobin

Nuria Plattner and Markus Meuwly
Department of Chemistry, University of Basel, Basel, Switzerland

ABSTRACT   The influence of electrostatic multipole moments up to hexadecapole on the dynamics of photodissociated carbon monoxide (CO) in myoglobin is investigated. The CO electrostatic potential is expressed as an expansion into atomic multipole moments of increasing order up to octopole which are obtained from a distributed multipole analysis. Three models with increasingly accurate molecular multipoles (accurate quadrupole, octopole, and hexadecapole moments, respectively) are developed and used in molecular dynamics simulations. All models with a fluctuating quadrupole moment correctly describe the location of the B-state whereas the sign of the octopole moment differentiates between the $Fe \cdots CO$ and $Fe \cdots OC$ orientation. For the infrared spectrum of photodissociated CO, considerable differences between the three electrostatic models are found. The most detailed electrostatic model correctly reproduces the splitting, shift, and width of the CO spectrum in the B-state. From an analysis of the trajectories, the spectroscopic B_1 and B_2 states are assigned to the $Fe \cdots CO$ and $Fe \cdots OC$ substates, respectively.

INTRODUCTION

The energetics, dynamics, and spectroscopic characterization of ligands in protein cavities provide fundamental information about intermolecular interactions and their role in controlling and influencing the relation between structure and function in proteins. Experimental and computational studies have revealed active sites within proteins which facilitate specificity for ligand binding and catalysis (1–4). Despite the remarkable progress in characterizing structural and dynamical aspects of ligands in protein active sites, the detailed (i.e., atomistic) and quantitative understanding of spectroscopic and kinetic data remains a central topic of biophysical research (5–7). One of the best studied examples, both experimentally and computationally, is the active site of myoglobin (Mb). Apart from its biological importance in storing and transporting dioxygen in the body, its involvement in vasodilation and in scavenging nitric oxide, Mb together with small diatomic ligands is a paradigm system for protein dynamics. Among these, photodissociated carbon monoxide (CO) from Mb is particularly well characterized. For this system, both structural and spectroscopic investigations for free CO in the heme pocket have been carried out (8–11).

Photodissociated CO in myoglobin is a system which has been investigated intensively by experiments (8–12) (low-temperature and time-resolved x-ray crystallography) and atomistic simulations (classical molecular dynamics (MD) and mixed quantum mechanical/molecular mechanics (QM/MM) MD simulations) (13–20). One general observation from all these efforts is that the details of the apparently simple processes of ligand dissociation and rebinding are

actually quite complex. For example, to correctly locate the docking site (B-state) where the CO molecule settles after breaking the Fe-CO bond in agreement with the experimental findings (8,9) it was necessary to carry out atomistic simulations with charge models which capture the quadrupole moment of CO (13,16). Another feature which has repeatedly attracted the attention of experimentalists (21) and theoreticians (14,15,22,23) alike, is the split infrared spectrum of photodissociated CO in the docking site which was originally observed by Anfinrud and co-workers (9,24). The IR spectrum of $Mb \cdots CO$ shows two well-resolved bands (at 2130.5 cm^{-1} and 2119.0 cm^{-1}), split by 11.5 cm^{-1}. Compared to free CO (2143.3 cm^{-1}), the upper band is shifted by ~ 10 cm^{-1} to the red whereas the lower band by ~ 20 cm^{-1} (24). The splitting has been associated with two possible orientations (states B_1 and B_2) of the CO molecule in the docking site, either with the carbon closer to the iron center (Fe–CO) or with the oxygen closer to the iron center (Fe–OC) (24). Some effort has gone into identifying the spectroscopic states B_1 and B_2 with either Fe–CO and Fe–OC. Originally, the two peaks have been assigned to Fe–CO (B_2) and Fe–OC (B_1) from an analysis of the rate of appearance of the two bands in polarization-sensitive experiments (25). Further studies were based on classical MD simulations (14,15), a combination of experiment and density functional theory (DFT) calculations on model compounds (21), MD simulations together with DFT and quantum bound state calculations (22) and simulations using the perturbed matrix method (23). The first two studies did not explicitly correlate one state with a particular IR band (14,15), whereas the next two studies (21,22) find that B_1 correlates with Fe–CO and B_2 with Fe–OC. This contrasts with an opposite assignment from recent PMM calculations (23).

It has been recognized for some time that the CO infrared spectrum in the B-state depends on the accurate representation

of the electrostatic interactions between CO and its environment (13–15). But even with a refined fluctuating quadrupolar model for CO which correctly describes the location of the B-state, the splitting of the IR spectrum, and the energetics for CO rotation (16), it was not possible to directly correlate one spectral feature with a particular orientation of the CO molecule relative to the heme-iron atom from MD simulations (26). In this work, we address the question whether a systematically improved description of the electrostatics around the CO molecule together with atomistic simulations can help us to quantitatively understand various aspects of CO dynamics in the B-state. In a conventional force field (27,28), the electrostatic potential is represented by point charges, which are often obtained from a population analysis of the Hartree-Fock wave function from ab initio electronic structure calculations (29). Usually, atom-centered charges are obtained by fitting atomic charges which optimally reproduce the electrostatic potential (30,31) or by adjusting the overall potential of reference systems to experimental data. Using atomic point charges to represent the electrostatics around a molecule is largely a matter of convenience, but is also supported historically. It has been demonstrated in the past, in the theory of population analysis algorithms, that point charges can be understood as a first term in a multipole expansion (32,33). Each term represents the corresponding multipole population of the ab initio electron-density distribution. The expansion converges toward the electrostatic potentials of the electron-density distribution on which the analysis is based.

For carbon monoxide (CO), two point charges are not sufficient to describe the electrostatic potential, because only the dipole moment, which is very small, can be reproduced accurately. In the past, different models have been developed to represent the conformationally dependent or independent dipole and quadrupole moment of CO accurately with respect to gas phase data (13,16,34). Furthermore, the influence of CO multipole moments in MD simulations of vapor-liquid equilibria of pure CO has been investigated using point dipole and point quadrupole moments obtained from fitting to thermodynamic data (35). In an earlier study (16), the splitting of the CO absorption band could be reproduced using a three-point fluctuating charge model for the description of the CO electrostatics. This study aims at systematically investigating the influence of higher electrostatic moments than the molecular quadrupole on the ligand-protein interaction in MbCO. In particular it is of interest to determine whether using a convergent mathematical expression for the electrostatic field around a ligand (CO) is directly related to a stepwise improvement of the observables (IR spectrum, probability density functions) calculated from them.

This work is structured as follows. First, the computational methods used are described. Next, results from simulations using increasingly detailed electrostatic models are presented. Finally, the results are discussed in view of experimental and previous computational work.

COMPUTATIONAL METHODS

Molecular dynamics simulations

The computational setup for the molecular dynamics (MD) simulations closely followed that of previous studies of photodissociated MbCO (16). Briefly, hydrogen atoms were added to the x-ray structure (Protein Data Bank reference 1MBC) (36), and the heme pocket was solvated by a 16 Å sphere of equilibrated water molecules. The reaction region of 12 Å was centered on the heme-Fe atom (see Fig. 1). The dynamics inside this region was described using Newtonian dynamics, the dynamics in the buffer region (12–16 Å) by Langevin dynamics. Friction coefficients of 62 ps^{-1} and 250 ps^{-1} were applied to the oxygen atoms of water and the remaining nonhydrogen atoms. Nonbonded interactions were treated with a cutoff at 10 Å. The sensitivity of the results on the cutoff for the nonbonded interactions has been tested on a subset of three trajectories, for which a nonbonded cutoff of 10 Å and 12 Å was used, respectively. Comparison of the averages over the three trajectories showed only minor differences. This is in agreement with findings from Meller and Elber who used particle-mesh Ewald techniques for the electrostatics (15). Bound MbCO was equilibrated for 70–140 ps before photodissociation which was modeled by the sudden approximation (37): The Fe-C bond was deleted and the bound parameters replaced by a repulsive term during 0.1 ps of dynamics. After this, the different electrostatic models were used for CO together with the CHARMM CO Van der Waals parameters and the RRKR bond potential for the CO stretching coordinate (38). For comparison of the different electrostatic models (A, B, C, and C′; see below), eight trajectories of 1 ns each were run and analyzed. For model C, which was found to be the most accurate, eight additional trajectories were evaluated. Simulations were carried out for both possible protonation states, His_δ 64 and His_ε 64. The latter is the more likely (39–41), although the former was used in several previous simulations (13,16) which also provided benchmarks for this work.

The infrared spectrum for each trajectory is calculated from the time dependence of the dipole moment of the CO molecule. The time correlation function is accumulated over 2^n time origins, where n is an integer such that 2^n corresponds to between 1/3 and 1/2 of the trajectory, with the time origins separated by 1 fs. This function can then be transformed to yield $C(\omega)$ using a
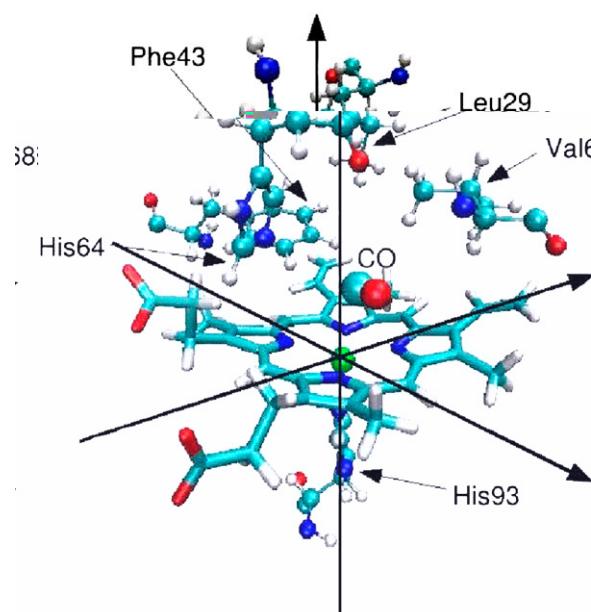

FIGURE 1 Myoglobin binding site together with the key residues and the CO molecule. The coordinate system is defined with respect to the iron center (*green sphere*) and the heme plane.

fast-Fourier transform with a Blackman filter to minimize noise (42). The final infrared adsorption spectrum is then calculated by evaluating

$$A(\omega) = \omega\{1 - \exp[-\omega/(kT)]\}C(\omega), \qquad (1)$$

where k is the Boltzmann constant and T is the temperature in Kelvin.

As a reference, the IR spectrum has also been calculated for free CO at 300 K using the RRKR potential. The spectrum shows one line at 2183 cm^{-1}. This corresponds to an offset of $\sim 40 \text{ cm}^{-1}$ compared to the experimental value which is consistent with previous investigations (16). The offset has two different origins. First, it has been noted from simulations of CO in argon (43) that the integration of the equations of motions using the Velocity-Verlet algorithm with a time step of 1 fs shifts the frequency by 16 cm^{-1}. The remaining 24 cm^{-1} can be attributed to the classical treatment of the anharmonic oscillator, which can be shown to have an energy-dependent fundamental frequency ω_E,

$$\omega_E = \alpha \sqrt{\frac{2(D_e - E_{tot})}{\mu}}, \qquad (2)$$

where E_{tot} is the total energy of the oscillator. All IR spectra discussed below are compared with the calculated spectrum for free CO (absorption at 2183 cm^{-1}).

Electrostatic models for CO

Multipole models

The distributed multipole algorithm (44) used here contains two different allocation methods for the multipole moments: the more localized basis functions are treated by a nearest-site algorithm. The less localized and diffuse basis functions are partitioned through space using the Lebedev integration method (45) over a spherical grid with 590 points. The atomic radii for this integration method are variable parameters. In this study, they have been adjusted such as to reproduce the molecular moments as accurately as possible for each model at the equilibrium C-O distance of 1.128 Å. Furthermore, the rank of multipoles is variable for each atom. Each molecular moment is composed of all atomic moments of lower and equal rank and was evaluated by using ORIENT (46).

Distributed multipoles are calculated using the program GDMA (44) based on Gaussian (47) formatted checkpoint files. Distributed multipoles for all models were evaluated for C-O distances $r \in [0.8..1.5]$ Å separated by 0.1 Å using the B3LYP functional and the aug-cc-pVQZ basis set (48,49). Different combinations of distributed multipoles on the two atoms have been evaluated, finally leading to three models (see Table 1). It was found that

distributed multipole analysis (DMA) faithfully reproduces the multipole moments of CO from high-level ab initio calculations (50,51) and experiment (see Fig. 2). Comparisons with other DFT methods and smaller basis sets showed that the molecular moments converge toward the values from B3LYP/aug-cc-pVQZ. The electrostatic potentials for the three models are represented as contour plots in Fig. 3. They show that the most important changes with increasing multipole order occur around the oxygen atom. In particular, whereas for the simplest model A only attractive interactions appear around the oxygen atom along the molecular axis, the more detailed model C has both attraction and repulsion. The changes of all atomic moments $q(r)$ as a function of the C-O bond length are to a good approximation linear. Therefore, they were described by linear functions $q(r) = \alpha + \beta(r - r_e)$ (see Fig. 4). Each atomic moment is defined by two parameters: its value α at the equilibrium bond length $r_e = 1.128$ Å and the slope β for the change with bond length. The coefficients of this linear expansion are given in Table 2.

Implementation of DMA

For the calculation of the atomic multipole moments, three additional multipole interaction terms in spherical tensor notation (52) have been implemented into CHARMM (27). A linear molecule (such as CO) can be oriented in a reference axis system for population analysis such that only the tensor components in z-direction (or in one arbitrary direction) are permanently populated. In the following, $q(00)$, $q(1z)$, $q(20)$, and $q(30)$ represent the charge and the z-components of the dipole, quadrupole, and octopole moment of atom sites a and b; R is the distance between the two atoms and
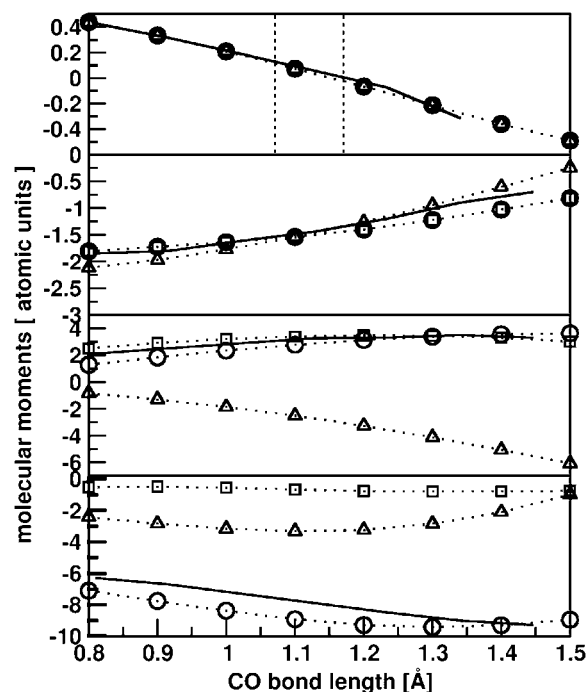
FIGURE 2 Molecular moments for the three electrostatic models for seven C-O bond lengths between 0.8 and 1.4 Å. (From *top* to *bottom*) Dipoles, quadrupoles, octopoles, and hexadecapoles. Model A is represented by triangles, model B by squares, and model C by circles. The solid lines represent the CCSD(T) values (50,51). Dipole and quadrupole moment are in good agreement with the ab initio data for all models. The octopole moment is accurately represented by models B and C; the hexadecapole moment from model C is the only one to qualitatively agree with the CCSD(T) calculations. The vertical lines represent the classical turning points for CO for $v_{CO} = 0$ with the RRKR potential.

TABLE 1 Molecular moments of CO calculated from the distributed multipoles on the C and O atom for models A–C

	Molecular moments				Highest atomic moment	
	$\mu[ea_0]$	$\Theta[ea_0^2]$	$\Omega[ea_0^3]$	$\Phi[ea_0^4]$	Carbon	Oxygen
Model A	0.04	−1.48	−2.68	−3.33	Dipole	Dipole
Model B	0.04	−1.51	3.42	−0.69	Dipole	Quadrupole
Model C	0.04	−1.51	2.86	−9.03	Quadrupole	Octopole
CCSD(T) (50, 51)	0.051	−1.47	3.46	−9.07		
Experiment*	0.048[†]	−1.58[‡]	4.15	−8.15		

The multipole moments (in atomic units) are evaluated for the equilibrium structure of CO.

*The values somewhat vary between experiments (for detailed information, see (50,51)).

[†]The experimental values have converged to this number.

[‡]This value varies between −1.4 and −1.68 ea_0^2 for different experiments.
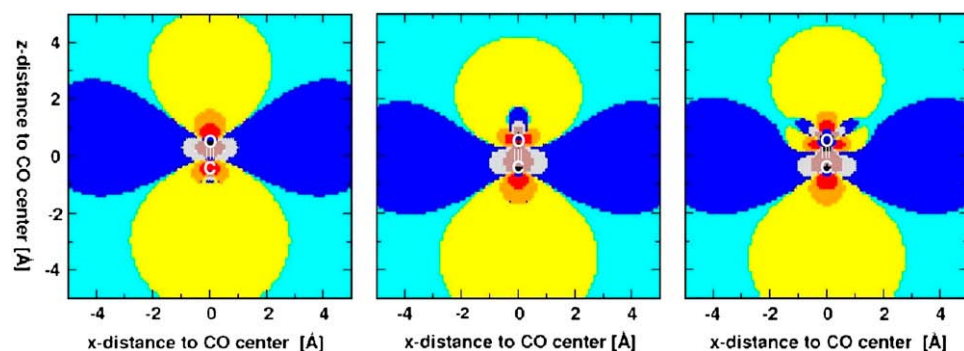
FIGURE 3 Electrostatic potentials for each of the three CO models. Model A (*left*), model B (*middle*), and model C (*right*). The colors mark the energy in kcal/mol of a probe charge of $1e$ interacting with the CO molecule, with the oxygen at $(0,0,0.564)$ Å and the carbon at $(0,0,-0.564)$ Å. Contours (in kcal/mol) are drawn for $E > 3$ (*brown*); $1.25 < E < 3$ (*gray*), $0.5 < E < 1.25$ (*blue*), $0 < E < 0.5$ (*cyan*), $0 < E > -0.5$ (*yellow*), $-0.5 < E > -1.25$ (*orange*), and $-1.25 < E < -3$ (*red*).

r_z^a is the direction cosine of a unit vector pointing from a to b. From the distributed multipoles on each site, the overall, molecule-centered multipoles are calculated with respect to the geometric center of the molecule using standard formulae (46). The geometric center is chosen instead of the center of mass to ensure that the electrostatic potential only depends on the electronic structure of a molecule; e.g., ^{14}CO and ^{15}CO should have the same molecular moments.

For the charge-dipole, charge-quadrupole, and charge-octopole interactions the contributions to the electrostatic interaction between site a on the CO molecule (described by DMA) and site b (which is an atom of the surrounding protein described by a point charge) is given by the following equations:

$$U_{(1z00)} = \frac{q(1z)_a q(00)_b r_z^a}{R^2}, \tag{3}$$

$$U_{(2000)} = \frac{q(20)_a q(00)_b (3(r_z^a)^2 - 1)}{2R^3}, \tag{4}$$

$$U_{(3000)} = \frac{q(30)_a q(00)_b (5(r_z^a)^3 - 3r_z^a)}{2R^4}. \tag{5}$$

For the simulations three different models are considered. Model A includes atomic multipoles up to the dipole on each atom (C and O, i.e., (dipole/dipole) on (C/O)), which allows us to accurately describe the quadrupole

moment of the CO molecule. Models B and C include (dipole/quadrupole) and (quadrupole/octopole) moments which give accurate values for the molecular octopole and hexadecapole, respectively. This data is summarized in Table 1. To obtain a more complete picture of the relationship between the convergent multipole expansion models and the trends in the corresponding observables, an additional model (C′) was considered which includes atomic moments up to octopole on both atoms. The molecular moments differ from model C only in the hexadecapole moment, which is $\Phi_{CO} = -6.855\ ea_0^4$ compared to $\Phi_{CO} = -9.025\ ea_0^4$ from model C.

RESULTS

As mentioned in Computational Methods, simulations are carried out for both protonation states of His-64 (His$_\delta$64 and His$_\varepsilon$64). The first part of this section presents results for His$_\delta$64 which can be directly compared to previous simulations which were based on the fluctuating charge model (13,16). In the second part, where comparison with experiment is made, results for His$_\delta$64 and His$_\varepsilon$64 are discussed.

Characterization of electrostatic models A–C

First, the influence of details of the electrostatic models on the localization and IR spectra of CO after photodissociation are presented. For this, eight independent 1-ns trajectories for each electrostatic model (A–C) are compared. Model C′ is not discussed in detail here because no significant differences to model C were found.

Orientational preference and location of the B-state

Initially, the orientation of CO in the docking site (B-state) was analyzed. The three electrostatic models differ mainly in their prediction of the CO-orientation with respect to the Fe atom which can be related to the difference $\delta = |r_{FeC_{CO}} - r_{FeO_{CO}}|$ between the iron-carbon and the iron-oxygen distance. Considering atom-atom distances is equivalent to transforming to spherical polar coordinates (θ, ϕ) but describes the quantity relevant in this work ("which CO-atom is closer to the Fe") more directly.

The results can be divided into three categories: orientations with carbon closer to iron (Fe···CO substate), orientations with oxygen closer to iron (Fe···OC substate), and
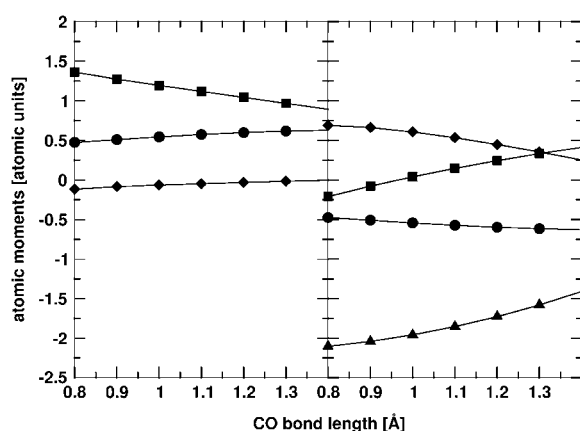

FIGURE 4 Atomic multipole moments for C-O bond lengths between 0.8 and 1.4 Å for model C. The left and right panels display the moments on the carbon and oxygen atom, respectively. Charges are marked by circles, dipoles by squares, quadrupoles by diamonds, and octopoles by triangles. The variation of the atomic moments with bond length is, to a good approximation, linear. This is also the case for the other two electrostatic models (not shown).

TABLE 2 Distributed multipole parameters for all electrostatic models

		Model A	Model B	Model C	Model C′
Charge[e]*	C	−0.563935[0.512792]	0.270293[0.227539]	0.563418[0.124576]	0.346638[0.073925]
Dipole[ea_0]	C	−0.226197[−0.581893]	0.818143[−0.431636]	1.096170[−0.395194]	0.880978[−0.151487]
	O	−0.955840[0.390026]	−0.180268[0.518313]	0.134258[0.5133167]	−0.104431[0.177545]
Quadrupole[ea_0^2]	C			−0.050725[0.087115]	−0.036699[−0.028279]
	O		0.562133[−0.324187]	0.467227[−0.453366]	0.624407[−0.087891]
Octopole[ea_0^3]	C				0.199193[0.197417]
	O			−1.774760[0.664064]	−1.239752[−0.048944]
Radius[Å]	C	0.500	0.660	0.700	0.800
	O	0.770	0.600	0.525	0.700

The values (α, [β]) refer to the equilibrium CO position and the linear changes (slope) of the moments as a function of the CO distance r (see main text). The units for the slopes are e/a_0, ea_0/a_0, ea_0^2/a_0, and ea_0^3/a_0, respectively. The radii are the relative atomic radii used for Lebedev integration in GDMA.
*Charges and changes of charge with bond length have opposite signs on oxygen.

orientations for which both distances are similar, which includes all distance differences $\delta \leq 0.3$ Å. The results (Fig. 5) show that models B and C clearly prefer the Fe···CO orientation, whereas model A prefers Fe···OC. This result does not only hold for the average orientation over all trajectories, but also for each individual trajectory. Comparison of the multipole moments in Table 1 shows that the major difference between model A and models B and C is the sign of the octopole moment Ω, which appears to determine the preferential orientation of unbound CO with respect to the Fe atom in the B-state. These findings are also in agreement with results from previous studies with a three-point fluctuating charge model with $\Omega = 0$, which makes it an intermediate case between models A and B/C. In MD simulations with the three-point fluctuating point charge model a less clear preferential orientation of CO in the B-state was found (16). The sensitivity of the results with respect to the criterion for distinguishing the substates was checked by using $\delta \leq 0.2$ Å, and no significant differences were found.

In addition to the relative orientation of the CO with respect to the heme-Fe atom it is also of interest to consider the CO probability distribution in the B-state. These distributions were analyzed in two ways. First, the center of mass of CO was projected onto the heme plane. These distributions (not shown) are similar to those from previous studies (16), with slight variations for the individual trajectories. All models find the docking site in a region between 3.5 to 4.5 Å away from the Fe atom and lined by residues His-64, Phe-43, and Val-68, which is consistent with experimental data from which it is known that shortly after photodissociation the CO molecule migrates to a metastable position (docking site or B-state) above the heme plane. Furthermore, the location of the CO molecule within the active site was characterized by considering the distance R between the geometric center of the CO and the Fe atom (see Fig. 5). All three models agree qualitatively for the distributions $p(R)$ with the exception that model C shows a higher proportion of large Fe–CO separations. Closer inspection of the trajectories reveals that these states correspond to CO positions in the Xenon-4 pocket. Models A–C and the previously developed fluctuating point charge model have a fluctuating quadrupole and correctly find the docking site whereas earlier work with a fixed three-point charge model showed some deficiencies in locating the B-state (16,53). In the x-ray structures the distance between the Fe atom and the geometric center of CO is 3.96 Å (PDB code 1DWS) (8) and 3.31 Å (PDB code 1AJH) (9), respectively.

In conclusion, it is found that a fluctuating quadrupole moment correctly describes the location of the B-state and
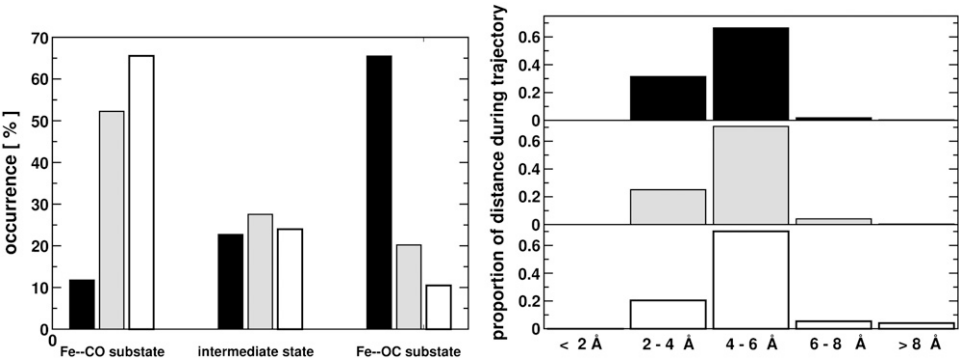

FIGURE 5 (*Left panel*) Orientations of the CO molecule for the three electrostatic models: model A (*solid*), model B (*shaded*), and model C (*open*). The Fe-C and Fe-O distances are compared at each step and divided into three categories: carbon closer to iron (Fe···CO substate), oxygen closer to iron Fe···OC substate), and distance differences $\delta <$ 0.3 Å (intermediate states). (*Right panel*) Distances of CO center of mass to the iron atom, calculated as the average of the Fe-C and Fe-O distance. The numbers indicate the distances at the center of each bin. The distances at ~8 Å correspond to positions in the Xenon-4 pocket.

the sign of the octopole moment differentiates between the Fe···CO and Fe···OC orientation.

Infrared spectra of dissociated CO

Structural data of unligated CO in Mb is quite rare (8,54,55), whereas the spectroscopic characterization provides more detailed information about the electrostatic environment of the ligand (11,24,25,56). Furthermore, because models B and C give essentially identical geometrical properties with respect to ligand orientation and the location of the B-state, it is of interest to investigate whether IR spectra are sensitive to higher-order multipole moments on the ligand. The experimental spectrum of photodissociated CO is split into two bands with different intensities, separated by 10 cm^{-1} and extending over ~20 cm^{-1} (full-width at half maximum, taken for each fitted Gaussian function separately). The more intense of the two bands (the one at higher frequency) is shifted to the red by 10 cm^{-1} relative to free CO (24).

In the following, the IR spectra from simulations with the three different electrostatic models (see Fig. 6) are discussed separately. The IR spectra are calculated from the autocorrelation function of the (fluctuating) dipole moment function along the trajectory according to Computational Methods (see above). Thus, the spectra displayed are directly comparable to experimental spectra and not power spectra. Differences between the models are characterized in terms of the shift with respect to free CO at 2183 cm^{-1}, the splitting of the

two bands, the bandwidths, and the relative band intensities. The results are summarized in Table 3.

Model A

The simplest model includes atomic multipoles up to the dipole on each atom. For this multipole model the Fe···OC orientation is preferred (see Fig. 5). The spectrum averaged over eight trajectories (*black line* in Fig. 6) is broad, extends from 2139 cm^{-1} to 2178 cm^{-1} (full-width at half maximum with respect to three Gaussian functions fitted to the spectrum) and does not show a clear splitting. The dominant peak is centered at ~2172 cm^{-1}. Together with the structural information from Fig. 5 (clear preference of Fe···OC over Fe···CO), this signal is tentatively assigned to the Fe···OC state.

Model B

This model includes atomic multipoles up to quadrupole. The frequency range is more narrow (full-width at half maximum from 2167 cm^{-1} to 2186 cm^{-1}) and the average spectrum shows a clear splitting. The vibrational band at higher frequency is not shifted with respect to free CO, in contrast to experiment (24). The splitting of the average spectrum is composed of the different shifts of the individual spectra and the spectra of single trajectories are either not split or show small splittings of ~4–10 cm^{-1}.

Model C

This model includes atomic multipoles up to octopole. The full-width at half maximum extends from 2153 cm^{-1} to 2184 cm^{-1}, which is intermediate between models A and B. The average spectrum shows a splitting and a shift of both bands compared to free CO, in qualitative agreement with the experimental data. Quantitatively, the shift is smaller (4 cm^{-1}) than the experimentally observed one (10 cm^{-1}). A more detailed analysis with additional data is given in
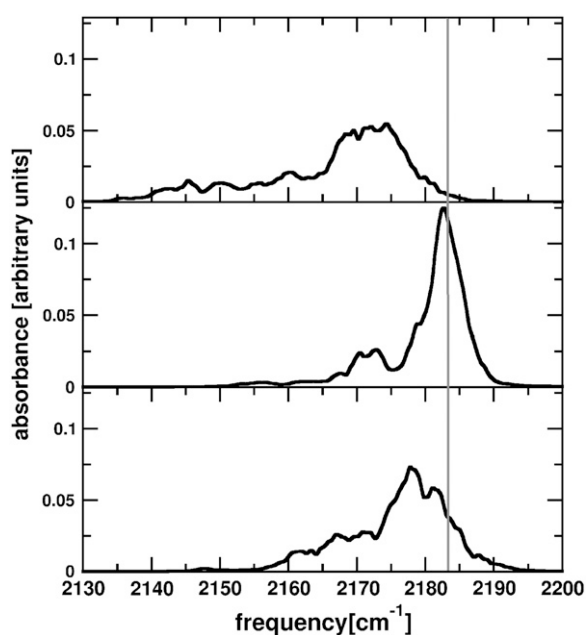

FIGURE 6   Average IR spectra over eight trajectories of 1 ns for each of the electrostatic models. The spectrum for model A (*top*) shows no clear splitting; broadening and red shift are too large. Model B (*center*) shows a splitting but no red shift compared to free CO. Model C (*bottom*) shows values for shifts and splitting in agreement with experiment. The shaded line indicates the frequency of free CO (2183 cm^{-1}).

TABLE 3   Characterization of the CO infrared spectra for the different electrostatic models

	His$_\delta$ 64			His$_\varepsilon$64	
	Model A	Model B	Model C	Model C	Exp. (24)
Splitting [cm^{-1}]	—	10.6	10.7 (13.8)	8.6	10
Shift [cm^{-1}]	11	0	4 (5)	3	10
Width [cm^{-1}]	39	19	31 (30)	32	32
Rel. intensities [%]	—	19	37 (46)	85	67

For His$_\delta$64 (model C), the number in brackets are averages over 16 trajectories, whereas for models A and B, the averages are over eight independent trajectories. For His$_\varepsilon$64 the averages are over 24 trajectories. The splitting is calculated from the fit to three Gaussian functions and the shift is reported for the band at higher frequency relative to free CO. Widths are full-widths at half maximum evaluated from the fit to three Gaussian functions. The relative band intensity is the maximum intensity of the band at lower frequency relative to the maximum intensity of the band at higher frequency.

the next section. In contrast to model B, the average splitting is the result of the splittings and shifts in the spectra of each individual trajectory, with splittings varying between 7 and 15 cm^{-1}.

Model C'

This model includes moments up to octopole on both atoms. It differs from model C only in the magnitude of the hexa-decapole moment. With a splitting of ≈ 14 cm^{-1}, a red shift of 6 cm^{-1}, and a width of 33 cm^{-1}, the spectrum is very similar to the one from model C (see Table 3). The deviations are within the range of statistical errors estimated from comparing the results from 8 and 16 trajectories for model C (Table 3). This suggests that the spectra are converged with respect to the multipole order on the ligand. Also, these values are in quite favorable agreement with the experimental data.

Additional evaluation for the most accurate electrostatic model

For model C, which most accurately describes higher multipole moments of CO, eight additional trajectories for His$_\delta$64 each 1 ns in length have been evaluated to better converge the average spectra. Based on this data, the relation between the dynamics of the CO molecule and the IR spectra has been analyzed. To characterize the differences between protonation at His$_\delta$64 and His$_\varepsilon$64, additional simulations (24 trajectories of 1 ns length) were carried out for the His$_\varepsilon$64 protonation with model C.

Relationship between CO orientation and absorption band intensities

It was already previously noted that extracting splittings in the wavenumber range in the IR spectrum from MD simulations alone may be difficult (15) and obscured through sampling of a multitude of substates which give rise to slightly different vibrational frequencies (26). Thus, in the following, an attempt is made to correlate structural aspects with spectroscopic features.

His$_\delta$64

Each of the 16 trajectories samples both substates (Fe···CO and Fe···OC) but with a different probability density for the two states according to the criterion (magnitude of δ) discussed in Orientational preference and location of the B-state. Thus, the 16 trajectories for model C have been divided into three groups. The first group (group I, least preference for Fe···CO) contained seven trajectories with <60% of the Fe···CO population, group II had six trajectories with between 60 and 70%, and group III (high Fe···CO preference) had three trajectories with >70% in the Fe···CO substate. Averages of the IR spectra have been calculated over all individual groups and three Gaussian functions were found to faithfully represent the average spectrum. The average over

trajectories with dominant Fe···CO preference (group III) shows mainly one broad band, whereas the average over group I (less pronounced Fe···CO preference, and therefore larger contributions of the Fe···OC substate) shows a clear splitting into two bands. The main peaks of the two states are separated by 13 cm^{-1}. In Fig. 7, the average spectrum from group I is compared to the average over all trajectories. Thus, the signal at lower wavenumber which only appears if the Fe···OC state is sufficiently populated, is assigned to the B$_2$ state. These findings are in accord with the identification of the two bands as the Fe···CO (B$_1$) and Fe···OC (B$_2$) substate (21,22) and are at variance with the recently published identification of the lower band as the Fe···CO substate and the higher band as the Fe···OC substate (see also Discussion) (23).

His$_\varepsilon$64

The analysis of the orientations of CO with respect to iron for His$_\varepsilon$64 showed a different distribution of the substates. The population for all three electrostatic models is shifted toward larger contributions of the Fe···OC substate, with model C showing only a moderate preference for the Fe···CO orientation. The 24 trajectories were again divided into three groups as follows:

Group I (least preference for Fe···CO) contains six trajectories with <30% Fe···CO.

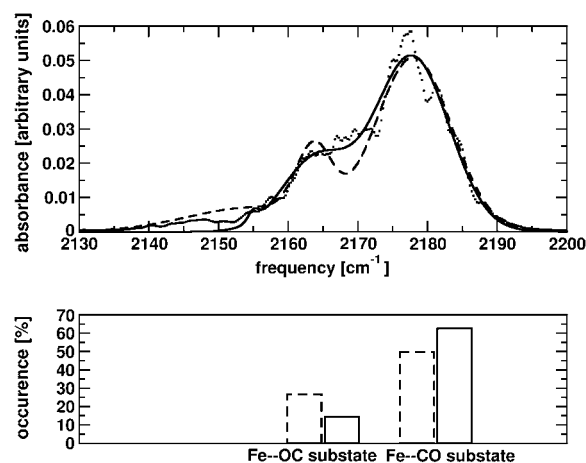Group II (intermediate) contains 12 trajectories.

FIGURE 7 His$_\delta$64: Relation between CO orientation with respect to iron and IR spectra. Average spectra are calculated over the seven trajectories with <60% of Fe···CO substate (group I, *dashed line*) and over all trajectories (*solid line*). The dotted line represents the raw (unfitted) data for the average over all trajectories. The sum of three Gaussian functions is fitted to the averages. The comparison shows that the shoulder at 2163 cm^{-1} of the average over all spectra can be identified with the Fe···OC substate, since it appears more pronounced in the dashed spectrum, where only trajectories with larger proportion of the Fe···OC substate are taken into account. The average percentage of each substate for the evaluated group I and for all trajectories is shown in the figure below. Dashed and solid lines in the diagram correspond to dashed and solid lines in the spectrum.

Group III (highest preference for Fe⋯CO) contains the remaining six trajectories with >42% of Fe⋯CO.

The averaged CO infrared spectra for each group are shown in Fig. 8. From this it is found that trajectories with a stronger preference for Fe⋯CO contribute more to the upper band (at 2180 cm^{-1}), whereas trajectories with a stronger preference for the Fe⋯OC orientations contribute more to the lower band (at 2172 cm^{-1}). This agrees with the findings for the His$_\delta$64 protonation state. The feature at ∼2155 cm^{-1} can be related to CO positions close and above the iron center with high contributions of the Fe⋯OC substate.

DISCUSSION AND CONCLUSION

In this study the influence of higher multipole moments on the dynamics and spectroscopy of photodissociated CO in the B-state of myoglobin has been systematically investigated. The CO molecule is described by atom-centered multipole moments on the carbon and the oxygen atom which were derived from a distributed multipole analysis (DMA). The protein environment, on the other hand, is treated with conventional point charges. For CO, three increasingly detailed charge models were used which differ in their ability to reproduce the experimentally known molecular multipole moments. Model A correctly describes the dipole and quadrupole moment, whereas model B reproduces the octopole moment and model C gives a satisfactory hexadecapole moment (with some deficiencies for the octopole moment).

The results from the MD simulations show that all models with fluctuating moments which correctly describe the

FIGURE 8 His$_\varepsilon$64: Relation between CO orientation with respect to iron and IR spectra. Averages are calculated over six spectra belonging to trajectories with the highest population of Fe⋯CO substate (solid line), six spectra belonging to trajectories with the highest population of Fe⋯OC substate (dashed), and over all trajectories (dotted). The sum over three Gaussian functions is fitted to each average. The average percentage of each substate for the evaluated groups is shown in the figure below. Dashed and solid lines in the diagram correspond to dashed and solid lines in the spectrum.

quadrupole moment are capable of locating the docking site (B-state) in agreement with experimental data. On the other hand, the average orientation of the CO molecule with respect to the heme-Fe atom (Fe–CO versus Fe–OC) in the B-state sensitively depends upon the sign of the octopole moment Ω. For the simplest model A, the Fe–OC substate is the dominant one, whereas with models B and C, Fe–CO is the more probable state. This is consistent with previous simulations (16) which were based on a fluctuating charge model with $\Omega = 0$ (i.e., intermediate between model A and models B/C) where it was found that the Fe–CO state is more stable.

One particular advantage of molecular dynamics simulations is that the infrared spectrum can be calculated directly from the Fourier transform of the dipole autocorrelation function. Such a procedure includes the full dynamics and treats the energetics and spectroscopy at an equal level. This is not the case for the combined MD/DFT/quantum bound state (22) and the PMM (23) calculations. All models used in this work correctly describe $\mu(r)$ over the range of r which is sampled in the vibrational ground and low excited states (see Fig. 2). Thus, the differences between the infrared spectra can be directly related to how CO interacts with its environment which, in turn, influences the space sampled by the photodissociated ligand. Contrary to previous efforts to relate structural and spectroscopic features (21–23), this work retains a maximum of information about the dynamically changing environment around the ligand. Earlier work related to this question suffers from different shortcomings. In the combined MD/DFT/quantum bound state work the frequency distribution was based on 50 snapshots. Although this number is considerable given the computational effort to determine the CO stretching potentials, some uncertainty remains as to the convergence of the results. However, a statistical analysis suggested that the principal findings should not change dramatically upon increasing the number of snapshots used (22). The PMM study included 21,000 snapshots at the expense of only using a minimal QM region (the CO molecule) which was treated with B3LYP/aug-cc-pVTZ whereas all other atoms were represented by point charges (23). This may influence the CO-vibrations because they depend on how well the interactions between CO and the nearby heme and His-64 residues are described. Such effects can also be seen in this study and are discussed below.

The extensive MD simulations for both protonation states (δ, ε) of His-64 lead to a split IR spectrum except for the simplest charge model A, which is the least reliable one. From grouping the trajectories using model C into those which sample the Fe–CO more (>70%) or less (<60%) extensively it is possible to relate the signal at lower wavenumbers to the Fe–OC conformation and the band at higher wavenumbers to the Fe–CO state. This is the assignment also found from the MD/DFT/quantum bound state calculations. Further (indirect) support for this assignment is provided by the IR spectrum from model A which predominantly samples the Fe–OC state (see Fig. 6). The corresponding IR spectrum
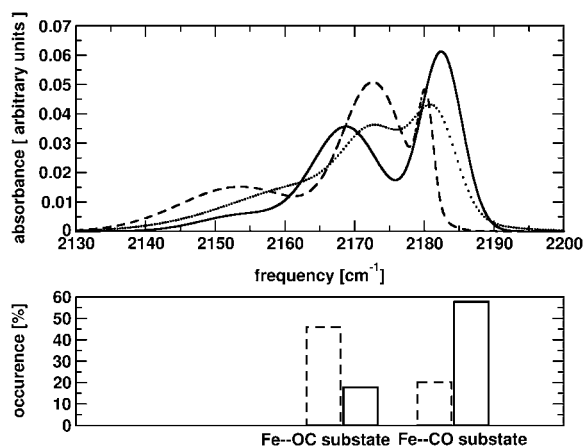
has a large peak in the wavenumber region (2170 cm^{-1}) where models B and C have their low-intensity bands. The calculated splitting from models B and C is between 8.6 and 12.8 cm^{-1}, depending on the protonation state of His-64. This is in very good agreement with experiment which finds a splitting of 10 cm^{-1}. Furthermore, the overall width and shape of the spectra correspond to the experimentally observed ones. The average over all spectra for Model C evaluated for His$_\delta$64 and His$_\varepsilon$64 is compared to the experimental spectrum (24) in Fig. 9. For His$_\delta$64, the intensity of the lower band is slightly weaker than in the experiment, the splitting is too large by ~3 cm^{-1} and the shift with respect to free CO is ~5 cm^{-1} smaller. For His$_\varepsilon$64, the intensity of the lower band is stronger than in the experiment, the splitting is too small by ~1 cm^{-1} and the shift with respect to free CO is ~7 cm^{-1} smaller. The overall widths and lineshapes of the spectra (flat at the red end and steep at the blue end) closely reflect those observed experimentally (see Fig. 9) and found in previous simulations (16) and differs from the almost symmetric lineshape found in the PMM simulations (23) which may be related to the small size of the QM region (CO molecule) and to the fact that the harmonic approximation was used in calculating the CO frequencies. For both His$_\delta$64 and His$_\varepsilon$64, the relative band intensities correctly find the lower band to be less intense than the band at higher frequency. Overall, the results for His$_\varepsilon$64 reflect the experimental data somewhat better than for His$_\delta$64. However, the difference between the results for His$_\delta$64 and His$_\varepsilon$64 does not only depend on the electrostatic model for the CO molecule, but also on the parameterization of the histidine residue. His-64 is described here by a conventional point charge model,
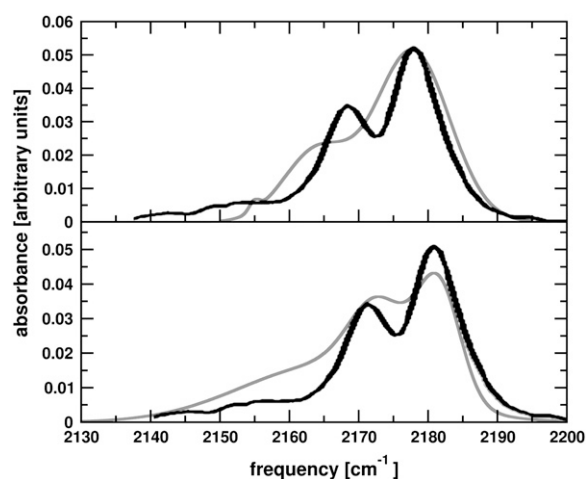
which may be insufficient to capture additional details of the two protonation states. This could be an explanation for the larger difference between the two states observed in previous QM/MM calculations including the CO molecule and the binding site environment in the quantum-mechanical part (22) where His-64 was treated quantum mechanically. To fully understand these discrepancies, more accurate descriptions of the entire binding site will be required.

One further comparison with experimental data can be made from these simulations. Using pump-probe experiments it has been observed that the center frequency of the CO stretch shifts as a function of time after photodissociation (11,57–59). This was attributed to the memory of the CO molecule of the bound state. Upon photodissociation, the CO fundamental frequency changes from ≈1950 cm^{-1} (bound or A-state) to ≈2130 cm^{-1} (unbound state). This change occurs on a timescale which is considerably longer than the photodissociation process itself. Experimentally, the spectra for times 0.3–100 ps after photodissociation (57) show a blue shift of ≈4 cm^{-1} whereas at longer times (10–100 ns after dissociation) the band shifts by another ≈2 cm^{-1} to the blue (11). From the simulations, the upper band of the IR spectrum at times 100 ps, 200 ps, 500 ps, and 1 ns after photodissociation is found to gradually shift to the blue by 10 cm^{-1}. The center frequency of the upper band is located at 2168 cm^{-1} after 100 ps and shifted to 2178 cm^{-1} at 1 ns, which is consistent with the experimental data for the high-frequency band (57). However, quantitatively the calculated blue shift of 10 cm^{-1} between 100 ps and 1 ns is too large. Possible reasons are the different quality of the stretching potential for bound and unbound CO and the fact that the electrostatic interaction between CO and the surrounding protein influences the stretching frequency. Furthermore, short dipole-dipole autocorrelation functions (for times early after photodissociation) are less reliable and lead to an artificial broadening of the spectra for short timescales. Thus, the uncertainty in the maximum absorption frequency is larger for early times compared to later times.

The IR spectra calculated for the different electrostatic models show a trend toward better agreement with experiment as the accuracy of the electrostatic models is improved. This is observed for the splittings, the red shifts with respect to free CO, the bandwidths, and the relative band intensities (Table 3). A comparison of all these features reveals that overall, model C, as the most accurate electrostatic model, shows the best agreement with experiment. Thus, it is found that using systematically improved descriptions of the electrostatics around CO yields improved calculations for structural and spectroscopic features of the CO dynamics in the main binding site of myoglobin.

FIGURE 9 Comparison of calculated and experimental spectra (Fig. 4 *B* from (24)). The computed spectra (*shaded*) are averages over 16 trajectories for His$_\varepsilon$64 (*top*) and 24 trajectories for His$_\varepsilon$64 (*bottom*). In both cases, three Gaussian functions have been fitted to the average spectrum. For direct comparison, the maximum of the high frequency band from the calculated and the experimentally observed spectrum (24) is separately aligned for both cases. The width and the splitting for the spectrum with His$_\varepsilon$64 better reproduces the experimental data.

REFERENCES

1. Williams, P., J. Cosme, and A. Ward. 2003. Crystal structure of human cytochrome P4502C9 with bound warfarin. *Nature*. 242:464–468.

2. Reibarkh, M., T. Malia, and G. Wagner. 2006. NMR distinction of single- and multiple-mode binding of small-molecule protein ligands. *J. Am. Chem. Soc.* 128:2160–2161.

3. Kraut, J., P. Sigala, B. Pybus, C. Liu, D. Ringe, G. Petsko, and D. Herschlag. 2006. Testing electrostatic complementarity in enzyme catalysis: hydrogen bonding in the ketosteroid isomerase oxyanion hole. *PLoS Biol.* 4:501–519.

4. Campbell, S., N. Gold, R. Jackson, and D. Westhead. 2003. Ligand binding: functional site location, similarity and docking. *Curr. Opin. Struct. Biol.* 13:389–395.

5. Kraut, J. 1988. How do enzymes work? *Science*. 242:533–540.

6. Wolfenden, R. 2003. Thermodynamic and extrathermodynamic requirements of enzyme catalysis. *Biophys. Chem.* 105:559–572.

7. Warshel, A., P. K. Sharma, M. Kato, Y. Xiang, H. B. Liu, and M. H. M. Olsson. 2006. Electrostatic basis for enzyme catalysis. *Chem. Rev.* 106:3210–3235.

8. Schlichting, I., J. Berendzen, G. Phillips, and R. Sweet. 1994. Crystal structure of photolyzed carbonmonoxy-myoglobin. *Nature*. 371:808–812.

9. Teng, T., V. Srajer, and K. Moffat. 1994. Photolysis-induced changes. *Nat. Struct. Biol.* 1:701–705.

10. Ostermann, A., R. Waschipky, F. Parak, and G. Nienhaus. 2000. Ligand binding and conformational motions in myoglobin. *Nature*. 404:205–208.

11. Schotte, F., M. Lim, A. Jackson, V. Smirnov, J. Soman, J. Olson, G. Phillips, M. Wulff, and P. A. Anfinrud. 2003. Watching a protein as it functions with 150-ps time-resolved x-ray crystallography. *Science*. 300:1944–1947.

12. Srajer, V., Z. Ren, T. Teng, M. Schmidt, T. Ursby, D. Bourgeois, C. Pradervand, W. Schildkamp, M. Wulff, and K. Moffat. 2001. Protein conformational relaxation and ligand migration in myoglobin: a nanosecond to millisecond molecular movie from time-resolved Laue x-ray diffraction. *Biochemistry*. 40:13802–13815.

13. Straub, J. E., and M. Karplus. 1991. Molecular dynamics study of the photodissociation of carbon monoxide from myoglobin: ligand dynamics in the first 10 ps. *Chem. Phys.* 158:221–248.

14. Ma, J., S. Huo, and J. Straub. 1997. Molecular dynamics simulation study of the B-states of solvated carbon monoxymyoglobin. *J. Am. Chem. Soc.* 119:2541–2551.

15. Meller, J., and R. Elber. 1998. Computer simulations of carbon monoxide photodissociation in myoglobin: Structural interpretation of the B states. *Biophys. J.* 74:789–802.

16. Nutt, D. R., and M. Meuwly. 2003. Theoretical investigation of infrared spectra and pocket dynamics of photodissociated carbonmonoxy myoglobin. *Biophys. J.* 85:3612–3623.

17. Nutt, D. R., and M. Meuwly. 2004. CO migration in native and mutant myoglobin: atomistic simulations for the understanding of protein function. *Proc. Natl. Acad. Sci. USA*. 101:5998–6002.

18. Bossa, C., M. Anselmi, D. Roccatano, A. Amadei, B. Vallone, M. Brunori, and A. Di Nola. 2004. Extended molecular dynamics simulation of the carbon monoxide migration in sperm whale myoglobin. *Biophys. J.* 86:3855–3862.

19. Danielsson, J., P. Banushkina, D. Nutt, and M. Meuwly. 2006. Computer simulations of structures, energetics and dynamics of myoglobin···ligand complexes. *Int. Rev. Phys. Chem.* 25:407–425.

20. Meuwly, M. 2007. Using small molecules to probe protein cavities: the myoglobin-XO (X = C, N) family of systems. *Eur. Phys. J.* 141:209–216.

21. Nienhaus, K., J. S. Olson, S. Franzen, and G. U. Nienhaus. 2005. The origin of stark splitting in the initial photoproduct state of MbCO. *J. Am. Chem. Soc.* 127:40–41.

22. Meuwly, M. 2006. On the influence of the local environment on the CO stretching frequencies in native myoglobin: assignment of the B-states in MbCO. *ChemPhysChem*. 10:2061–2063.

23. Anselmi, M., M. Aschi, A. Di Nola, and A. Amadei. 2007. Theoretical characterization of carbon monoxide vibrational spectrum in sperm whale myoglobin distal pocket. *Biophys. J.* 92:3442–3447.

24. Lim, M., T. A. Jackson, and P. A. Anfinrud. 1995. Mid-infrared vibrational spectrum of CO after photodissociation from heme: evidence of a docking site in the heme pocket of hemoglobin and myoglobin. *J. Chem. Phys.* 102:4355–4366.

25. Lim, M., T. A. Jackson, and P. A. Anfinrud. 1997. Ultrafast rotation and trapping of carbon monoxide dissociated from myoglobin. *Nat. Struct. Biol.* 4:209–214.

26. Nutt, D., P. Banushkina, and M. Meuwly. 2005. Computational chemistry for elucidating protein function: Energetics and dynamics of myoglobin-ligand systems. *Chimia (Aarau)*. 59:517–521.

27. MacKerell, A. D., Jr., D. Bashford, M. Bellott, R. L. Dunbrack, Jr., J. D. Evanseck, M. J. Field, S. Fischer, J. Gao, H. Guo, S. Ha, D. Joseph-McCarthy, L. Kuchnir, K. Kuczera, F. T. K. Lau, C. Mattos, S. Michnick, T. Ngo, D. T. Nguyen, B. Prodhom, W. E. Reiher III, B. Roux, M. Schlenkrich, J. C. Smith, R. Stote, J. E. Straub, M. Watanabe, J. Wiorkiewicz-Kuczera, D. Yin, and M. Karplus. 1998. All-atom empirical potential for molecular modeling and dynamics studies of proteins. *J. Phys. Chem. B*. 102:3586–3616.

28. Weiner, S. J., P. A. Kollman, D. A. Case, U. Singh, C. Ghio, G. Alagona, S. Profeta, Jr., and P. Weiner. 1984. A new force-field for molecular mechanical simulation of nucleic-acids and proteins. *J. Am. Chem. Soc.* 106:765–784.

29. Mulliken, R. 1955. Electronic population analysis on LCAO-MO molecular wave functions. *J. Chem. Phys.* 23:1833–1840.

30. Singh, U. C., and P. A. Kollman. 1984. An approach to computing electrostatic charges for molecules. *J. Comput. Chem.* 5:129–145.

31. Besler, B. H., K. M. Merz, and P. A. Kollman. 1990. Atomic charges derived from semiempirical methods. *J. Comput. Chem.* 11:431–439.

32. Stone, A. J., and M. Alderton. 1985. Distributed multipole analysis—methods and applications. *Mol. Phys.* 56:1047–1064.

33. Sokalski, W., and R. Poirier. 1983. Cumulative atomic multipole representations of the molecular charge distribution and its basis set dependence. *Chem. Phys. Lett.* 98:86–92.

34. Mankoo, P. K., and T. Keyes. 2006. Induction model for molecular electrostatics: application to the infrared spectroscopy of CO liquid. *J. Chem. Phys.* 124:204503.

35. Stoll, J., J. Vrabec, and H. Hasse. 2003. A set of molecular models for carbon monoxide and halogenated hydrocarbons. *J. Chem. Phys.* 119:11396–11407.

36. Kuriyan, J., S. Wilz, M. Karplus, and G. Petsko. 1986. X-ray structure and refinement of carbon-monoxy (Fe-II)-myoglobin at 1.5-Å resolution. *J. Mol. Biol.* 192:133–154.

37. Meuwly, M., O. Becker, R. Stote, and M. Karplus. 2002. NO rebinding to myoglobin: a reactive molecular dynamics study. *Biophys. Chem.* 89:183–207.

38. Huffaker, J. N. 1976. Diatomic molecules as perturbed Morse oscillators. I. Energy levels. *J. Chem. Phys.* 64:3175–3181.

39. Johnson, J., D. Lamb, H. Frauenfelder, J. Muller, B. McMahon, G. Nienhaus, and R. D. Young. 1996. Ligand binding to heme proteins. 6. Interconversion of taxonomic substates in carbonmonoxymyoglobin. *Biophys. J.* 71:1563–1573.

40. Rovira, C., B. Schulze, M. Eichinger, J. D. Evanseck, and M. Parrinello. 2001. Influence of the heme pocket conformation on the structure and vibrations of the Fe-CO bond in myoglobin: a QM/MM density functional study. *Biophys. J.* 81:435–445.

41. Merchant, K. A., W. G. Noid, D. E. Thompson, R. Akiyama, R. F. Loring, and M. D. Fayer. 2003. Structural assignments and dynamics of the A substates of MbCO: spectrally resolved vibrational echo experiments and molecular dynamics simulations. *J. Phys. Chem. B*. 107:4–7.

42. Allen, M. P., and D. J. Tildesley. 1987. Computer Simulation of Liquids. Clarendon Press, Oxford.

43. Berens, P. H., and K. R. Wilson. 1981. Molecular-dynamics and spectra. 1. Diatomic rotation and vibration. *J. Chem. Phys.* 74:4872–4882.

44. Stone, A. J. 2005. Distributed multipole analysis: stability for large basis sets. *J. Chem. Theory Comput.* 1:1128–1132.

45. Lebedev, V., and D. N. Laikov. 1999. Quadrature formula for the sphere of 131th algebraic order of accuracy. *Dokl. Math.* 59:477–481.

46. Stone, A. J., A. Dullweber, O. Engkvist, E. Fraschini, M. P. Hodges, A. W. Meredith, D. R. Nutt, P. L. A. Popelier, and D. J. Wales. 2002. ORIENT: a program for studying interactions between molecules. Available at http://www.stone.ch.cam.ac.uk/programs.html#Orient.

47. Frisch, M. J., G. W. Trucks, H. B. Schlegel, G. E. Scuseria, M. A. Robb, J. R. Cheeseman, J. A. Montgomery, Jr., T. Vreven, K. N. Kudin, J. C. Burant, J. M. Millam, S. E. S. Iyengar, J. Tomasi, V. Barone, B. Mennucci, M. Cossi, G. Scalmani, N. Rega, G. A. Petersson, H. Nakatsuji, M. Hada, M. Ehara, K. Toyota, R. Fukuda, J. Hasegawa, M. Ishida, T. Nakajima, Y. Honda, O. Kitao, H. Nakai, M. Klene, X. Li, J. E. Knox, H. P. Hratchian, J. B. Cross, C. Adamo, J. Jaramillo, R. Gomperts, R. E. Stratmann, O. Yazyev, A. J. Austin, R. Cammi, C. Pomelli, J. W. Ochterski, P. Y. Ayala, K. Morokuma, G. A. Voth, P. Salvador, J. J. Dannenberg, V. G. Zakrzewski, S. Dapprich, A. D. Daniels, M. C. Strain, O. Farkas, D. K. Malick, A. D. Rabuck, and K. Raghavachari. J. B. F. Resman, J. V. Ortiz, Q. Cui, A. G. Baboul, S. Clifford, J. Cioslowski, B. B. Stefanov, G. Liu, A. Liashenko, P. Piskorz, I. Komaromi, R. L. Martin, D. J. Fox, T. Keith, M. A. A. Laham, C. Y. Peng, A. Nanayakkara, M. Challacombe, P. M. W. Gill, B. Johnson, W. Chen, M. W. Wong, C. Gonzalez, and J. A. Pople. 2004. Gaussian 03, Rev. C.01. Gaussian Incorporated, Wallingford, CT.

48. Becke, A. D. 1993. Density-functional thermochemistry. 3. The role of exact exchange. *J. Chem. Phys.* 98:5648–5652.

49. Dunning, T. H., Jr. 1989. Gaussian-basis sets for use in correlated molecular calculations. 1. The atoms boron through neon and hydrogen. *J. Chem. Phys.* 90:1007–1023.

50. Maroulis, G. 1996. Electric polarizability and hyperpolarizability of carbon monoxide. *J. Phys. Chem.* 100:13466–13473.

51. Maroulis, G. 2001. Accurate higher electric multipole moments for carbon monoxide. *Chem. Phys. Lett.* 334:214–219.

52. Stone, A. J. 1996. The Theory of Intermolecular Forces. Clarendon Press, Oxford, UK.

53. Vitkup, D., G. A. Petsko, and M. Karplus. 1997. A comparison between molecular dynamics and x-ray results for dissociated CO in myoglobin. *Nat. Struct. Biol.* 4:202–208.

54. Teng, T., V. Srajer, and K. Moffat. 1997. Initial trajectory of carbon monoxide after photodissociation from myoglobin at cryogenic temperatures. *Biochemistry.* 36:12087–12100.

55. Vojtechovsky, J., K. Chu, J. Berendzen, G. Phillips, R. Sweet, and I. Schlichting. 1999. Crystal structures of myoglobin-ligand complexes at near-atomic resolution. *Biophys. J.* 77:2153–2174.

56. Phillips, G., M. Teodoro, T. Li, B. Smith, and J. Olson. 1999. Bound CO is a molecular probe of electrostatic potential in the distal pocket of myoglobin. *J. Phys. Chem. B.* 103:8817–8829.

57. Kim, S., and M. Lim. 2005. Picosecond dynamics of ligand interconversion in the primary docking site of heme proteins. *J. Am. Chem. Soc.* 127:5786–5787.

58. Lin, M., T. A. Jackson, and P. Anfinrud. 2004. Orientational distribution of CO before and after photolysis of MbCO and HbCO: a determination using time-resolved polarized mid-IR spectroscopy. *J. Am. Chem. Soc.* 126:7946–7957.

59. Anfinrud, P., M. Lim, and T. Jackson. 1994. Femtosecond IR spectroscopy: methods and applications to protein dynamics. *Proc. SPIE Int. Soc. Opt. Eng.* 2138:107–115.